Collimation and energy enhancement in laser driven MeV protons

K. Makur, [ID] S. Krishnamurthy, [ID] and B. Ramakrishna[a] [ID]

AFFILIATIONS

Department of Physics, Indian Institute of Technology Hyderabad, Kandi, Sangareddy 502285, India

[a]Author to whom correspondence should be addressed: bhuvan@phy.iith.ac.in

ABSTRACT

Enhancing the energy and controlling the divergence of proton beam have been crucial tasks since the development of laser-based ion accelerators. In this study, we employ 2D particle-in-cell EPOCH simulation to investigate a method to control the divergence and enhance the energy of MeV proton beam produced from the interaction of high intensity laser with a gold target. The energy and divergence of proton beam for the conventional laser-foil target configuration are compared with our proposed three laser-three target configuration. In the single laser-single target configuration, a high intensity laser irradiates a gold foil target resulting in proton acceleration from the plasma. In contrast, in the three laser-three target configuration, the generated proton beam is allowed to traverse through the configuration of two parallel Al plates irradiated with high intensity lasers. The new configuration provides the proton energy enhancements of 40% and more collimated beam compared to the single laser-foil target setup. This collimation and energy increase are due to the vertical and horizontal components of the electric field generated by the hot electron plasma of Al plates. The proton energy and divergence can also be tuned by varying the plasma electron density of the Al plasma. Also, the control of proton beam collimation is explored by varying target parameters as well, and it is observed that the separation between the Al plates and length of the Al plates plays major role in controlling the divergence of the beam. This study will have a significant impact in the ongoing laser fusion program, fast ignition, and laser ion therapy.

Published under an exclusive license by AIP Publishing. https://doi.org/10.1063/5.0134619

INTRODUCTION

The interaction of the high intensity laser ($I > 10^{18}$ W cm^{-2}) with matter is a promising source for electrons,[1] ions,[2–4] x rays,[5,6] and different radiation[7] through the production of hot-dense plasma. Due to its low cost, reduced source size, high beam densities, and short pulse duration typically in the picosecond range, the laser-based accelerator provides substantial benefits over the conventional accelerator. Ion (proton) acceleration in the MeV ranges[8–10] from the laser plasma interaction has attracted great attention for various applications, such as proton therapy,[11–13] proton radiography,[14–16] and fast ignition in inertial confinement fusion.[17] In view of the many potential applications stated earlier, the energy and beam divergence must be properly optimized. Target normal sheath acceleration (TNSA), radiation pressure acceleration (RPA), and shock acceleration are a few of the mechanisms used to produce ions with relativistic energy, with the currently available intensity ($I > 10^{18-21}$ W cm^{-2}). Ion acceleration from the TNSA is one of the most frequently investigated mechanisms. In the TNSA process,[18–20] hot electrons generated at the target's front surface travel through the target, creating a charge separation between heavy ions and electrons as they reach the target's backside, resulting in a strong sheath of an electric field in the range of TV/m.[21] This strong electric field further accelerates the proton from the contaminant layers of hydrocarbon present at the rear side of the target.[22,23] The maximum proton energy and the divergence of the beam solely depend on the fast electron propagation and the produced sheath field at the rear side of the target,[24] and any deformation in the sheath field will lead to a perturbation in the proton beam. The fast electron propagation is smooth until it reaches the Alfvén current limit ($I_A \sim 17~\beta\Upsilon$ kA),[25] to maintain a continuous flow of any current exceeding the Alfvén limit, a return current must flow to counter balance the forward current,[26,27] and the imbalance between these two currents produces a magnetic field that makes the fast electron transportation complicated leading to inhibition to the electron beam flow.[28,29] These filamentary structures are imprinted on the proton beam because the proton is driven by the sheath field created by the fast electrons,[30] and this disruption of the sheath field increases the divergence of the beam and lowers the proton peak energy as well. The divergence of the proton beams due to the different instabilities is inherent in nature, and proper control should be achieved for the application purposes. A low divergence proton beam is necessary,

especially in proton fast ignition and cancer therapy. The location and size of the cancer cells determine the energy and divergence of the proton beam required for cancer therapy. A larger divergent proton beam can potentially cause damage to healthy tissues. In the case of inertial confinement fusion, for the proton fast ignition[31] to occur, a highly energetic proton beam with high flux should deliver the energy on the pre-compressed D–T fuel to start the ignition process.

The TNSA field produced proton beam is poly-energetic in nature due to the Gaussian sheath field distribution. The lower energy particles will have higher divergence in comparison with higher energy particles. The proton beam energy and the beam collimation are very much correlated, since the distortion of the sheath field not only makes the proton beam divergent but also produces a low energetic proton beam. In the past, the focus has been primarily on reducing instabilities by smoothing the sheath field, which is accomplished by controlling fast and return current propagation employing sandwich targets of resistive gradients. The collimation of the hot electrons, which is reflected in the proton beam divergence, is caused by the strong self-generated resistive field at the interface of the resistive gradient.[32–34] The beam quality will deteriorate in terms of energy and collimation if the sheath field has a large spread along the transverse direction. In the work of Sonobe et al.[35] and Yu et al.,[36] they have demonstrated that one may regulate the sheath field by localizing the electrons, which limits the transverse spread of the electron beam. This is accomplished by drilling a hole in the back of a slab target, opposite to the laser irradiation point. In another attempt to smoothen the sheath field, the work of Gong et al.[37] showed that a target with density gradient can be an effective way to control the beam divergence. In their structured target, a core with low electron density and a cladding with higher electron densities are used. In this configuration, the laser propagation becomes stable and is effectively guided along the core. The smooth propagation of the laser along the core channel results in a smooth distribution of electrons at the end of the core channel, generating a smooth sheath field for proton acceleration. Also, different target geometries like curvature targets[38,39] and quadrupole magnets[40–42] are seen to be used for controlling the angular distribution of the proton beam. Another novel method for collimating the proton beam is the micro lens,[43,44] in which a strong sub picosecond laser pulse irradiates a hollow cylinder, and the divergence is reduced by the triggered transient field on the inside wall of the cylinder as it passes through the cylinder, but the energy enhancement is not addressed.

Several works have been reported on the proton energy enhancements. Increasing the laser pulse absorption by electrons is essential in improving the transfer of laser energy to ions. The experiment performed by the Strehlow et al.[45] showed how attaching a microtube at the front side of a slab target increases the laser absorption by the electrons, which, in turn, increases the proton peak energy. The work of Gizzi et al.[46] shows the inclusion of micrometer ranged pre-plasma can be an effective way to increase the proton cutoff energy. Eventually, different pre-plasma scale length changes the laser absorption and modifies the behavior of the fast electrons.

Thus far, the primary focus has been to smoothen the sheath field to gain control over the proton beam. In this work, instead of improving the beam quality in terms of energy and collimation inherently, our focus is to gain control over the proton beam externally after the protons are accelerated from the rear side of the gold foil target. In this scheme, the aluminum foils upon interaction with two separate laser pulses would provide the strong electric field that acts to collimate the proton beams as well as to accelerate further, so that the proton energy is also increased. The proposed scheme offers flexibility in parameter selection to enhance energy and collimate proton beams by adjusting the secondary laser parameters, length and spacing of aluminum plates, and aluminum plasma density. The uniqueness of this approach lies in the simultaneous focusing as well as energy enhancement in the proton beam in a single setup. Up to 40% increase in proton energy is observed in the proposed scheme as compared to a conventional slab target.

SIMULATION SETUP

Particle-in-cell (PIC) 2D simulations were performed using the open-source code EPOCH.[47] The simulation box extends from -15 to $+25\,\mu m$ along the x direction and -12 to $+12\,\mu m$ along the y direction. With the grid size of $10\,nm$ in both directions, the number of grid cells was kept at 4000 and 2400 along the x and y directions, respectively. The number of macroparticles in a single cell is 32 for both ions and electrons. The two configurations addressed in this work, single laser–single (SS) target configuration and three laser–three target configuration (TT), are referred to as S–S and T–T, respectively, throughout the discussion. The first laser is allowed to propagate from the –X direction, and another two (second and third) lasers are allowed to propagate from the $+Y$ and –Y directions [Fig. 1(b)]. For all three lasers, P polarized Gaussian profile with a wavelength of $1\,\mu m$ and pulse duration of 50 fs (FWHM) is used. The peak intensity for the first laser (used to accelerate protons) is taken to be 4×10^{20} W cm^{-2}, whereas for the second and third laser (used for collimation of protons), it is 3×10^{19} W cm^{-2}, with a focal spot of FWHM is $2.5\,\mu m$ for all three lasers. A gold (Au) target of a thickness of $2\,\mu m$ is placed at X $= -15\,\mu m$, whereas two parallel plates of aluminum of a thickness of $2\,\mu m$ separated by $10\,\mu m$ were kept parallel to the X axis, as shown in Fig. 1(a). We label the lasers into three names for our convenience: Laser 1—which is the primary laser interacting with the Au target and has an intensity of 4×10^{20} W cm^{-2}, laser 2—the secondary laser with intensity is 3×10^{19} W cm^{-2} propagating from the $+Y$ direction and interacting with the top Al plate, and laser 3—another secondary laser with the intensity same as laser 2 propagating from the $-Y$ direction and interacting with the bottom Al plate. We named the two regions as up region and down region, and the up region is the region between Y $= 0$ axis and the upper Al plates, and the down region is defined as the region between the Y $= 0$ axis and the down Al plate. Figure 1(b) depicts these two zones, which are mirror symmetric with respect to the Y $= 0$ axis. We initialized both the target with a fully ionized plasma with the electron density for the Au and Al targets being 54 and $10n_c$, respectively, where n_c is the critical density, $n_c = (\epsilon_0 m_e w_0^2)/(4\pi e^2)$, where $w_0 = 2\pi c/\lambda_0$ is the angular frequency corresponding to the laser wavelength (λ_0) and ϵ_0, m_e, and e are the free space permittivity, mass of the electron, and electron charge, respectively. We chose to use an ionized target due to computational limitations. Preliminary simulations using a un-ionized gold target of equal thickness and a laser pulse with identical parameters yielded ionization states up to 75+, with a significant proportion. Thus, considering a fully ionized target is a reasonable choice in light of computational constraints. In our simulation, the electron density for the Al target varied from low density to solid density (10 to $52n_c$) to
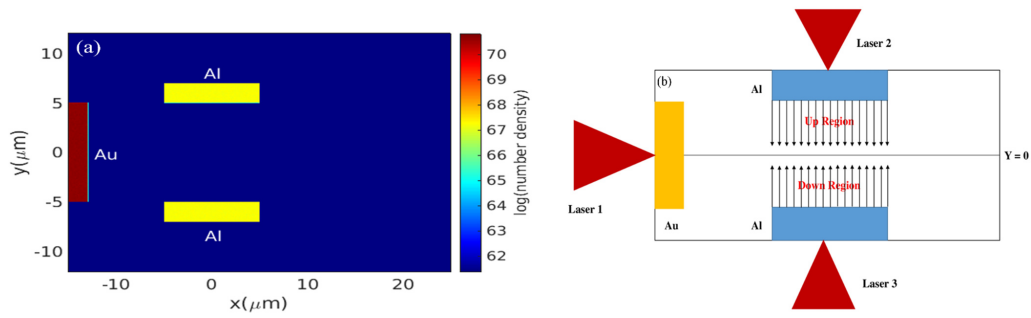
FIG. 1. (a) Simulation set up with the overall density of three targets (Gold and two parallel Al targets) is shown here. (b) The schematic layout for the simulation setup; the up region is defined as the region between the Y = 0 axis and the upper Al plate, whereas the down region is referred to as the region between Y = 0 axis and the lower Al plate, and the arrows represent the schematic electric field lines.

observe the effect of plasma density on the laser absorption, while the gold target density is kept constant at $54n_c$. Since the proton from the contaminant layer gets accelerated in the TNSA electric field, a 50 nm proton layer is coated on the rear side of the gold target for all the configurations.

RESULTS

We report the divergence control and energy enhancement of the proton beam for both of our configurations: S–S configuration and T–T configuration. In the S–S configuration, the proton beams generated from the Au gold target of thickness $2\,\mu m$ upon interacting with a 50-fs laser pulse of intensity $I = 4 \times 10^{20}$ W cm^{-2}, whereas in the T–T configuration, the same proton beam generated from the Au

target is allowed to traverse through the two parallel Al plates interacting with another two lasers with an intensity of $I = 3 \times 10^{19}$ W cm^{-2}. The Al plates have dimensions of $2\,\mu m$ in thickness and $10\,\mu m$ in length, and they are separated by a $10\,\mu m$ distance. Figures 2(a) and 2(b) show the proton beam energy distribution from the Au target for the S–S and T–T configurations, respectively. These snapshots are taken a 500 fs, that is after the proton beams come out of the Al plates region and reach the end of the simulation box. Figures 2(c) and 2(d) show momentum (P_x) distribution of the proton beam for both the configurations. The poly-energetic beam profile for both the cases with maximum proton energies of 30 and 42 MeV, respectively, for S–S and T–T configurations is observed. The energy enhancement is studied in greater detail and these results show that the proton beams
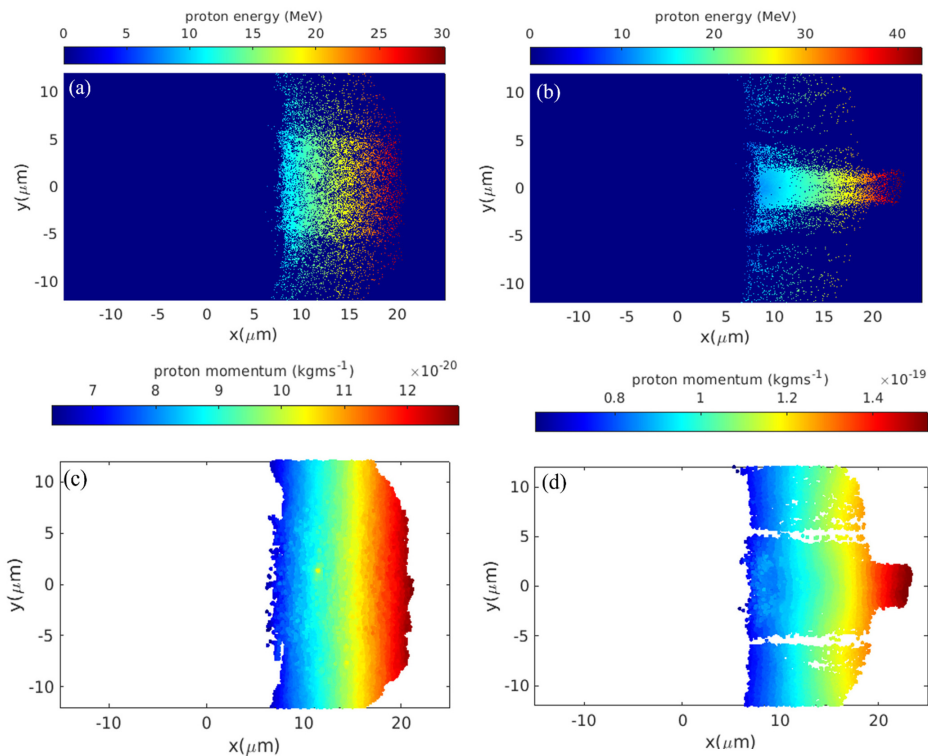

FIG. 2. Energy and momentum distribution for the proton beam generated from Au target at 500 fs; (a) and (b) correspond to the proton energy beam profile for the S–S and T–T configurations, respectively, and (c) and (d) correspond to the momentum (P_x) distribution for S–S and T–T configurations, respectively.

are more collimated in the case of T–T configuration compared to S–S. By comparing the energy distribution and momentum distribution (P_x) of these two cases, we can infer the proton beam is more convergent in the case of the T–T configuration compared to the S–S configuration. Upon comparing the momentum distributions for both cases, a noticeable white gap is observed in the T–T configuration [Fig. 2(d)]. Interestingly, this white gap appears only after the protons have entered the region between the Al plates, as confirmed by the simulation. This phenomenon is primarily attributed to the strong focusing effect near the Al plate surfaces. Specifically, protons that are situated in proximity to the Al target surface experience a greater push toward the center of the region, resulting in their displacement toward the same. As a result, the displacement of these protons close to the Al plate surfaces manifests as a gap in the momentum distribution. In both of our cases, the proton is generated from the same gold target, but the same proton beam while passing through the region of two plates interacting with another two lasers makes the proton beams collimated. The physical reason behind this is as follows: after irradiation of the two lasers with the two Al plates, the generated hot electrons at critical density surface penetrate through the plates and quickly spread across the interior of the Al plates. These electrons initially condense over a Debye length on the surface of the plate and produce a space charge sheath field. The sheath field created by these hot electrons is large enough to ionize the Al plates resulting in hot plasma expansion. The resultant transient electric field produced at each Al plate surface is propagated toward the center of the region between the two plates by the action of plasma expansion. Since the field acts toward the center, protons undergo focusing.

The generated protons from the Au target have some inherent divergence angle; nevertheless, for this beam to be focused, there should be some electric field component strong enough to generate the necessary Lorentz force for pushing the beam toward the $Y = 0$ direction and making the proton beam more convergent. To understand the impact of the electric field on the collimation of the proton beam, we have calculated the average electric field E_y in the up region and the down region for both the S–S and T–T configurations. Figure 3 compares the average electric field E_y calculated in the up region and down region for both the configurations (S–S and T–T). The average E_y field in both the region is random in nature for the case of the S–S configuration, and it is almost close to the zero electric field line. This zero electric field for the S–S configuration indicates the no focusing effect, which is already reflected in the proton beam profile shown in Fig. 2(a). In the case of (T–T) configurations, a strong electric field of the order of 10^{11} V/m is observed for both the region, and they are directed opposite each other facing toward $Y = 0$. The average electric field in the down region is in the positive Y direction, whereas it is in the negative Y direction for the up region. For proton to be focused due to this E_y field, the electric field direction should be in the negative Y direction in the up region due to the upper plate, and it should be in the positive Y direction in the down region due to the lower Al plate, which is already reflected in the simulated electric field for both the regions (Fig. 3). Focusing can only be possible if there is some resultant electric field available in both regions (up region and down region). The electric field variation in Fig. 3 is transient in nature with time; once two secondary lasers begin interacting with the Al plates, hot electrons are expelled out leading to the generation of the electric field. Since this electric field is proportional to the number of electrons, the electric field grows till the electrons are
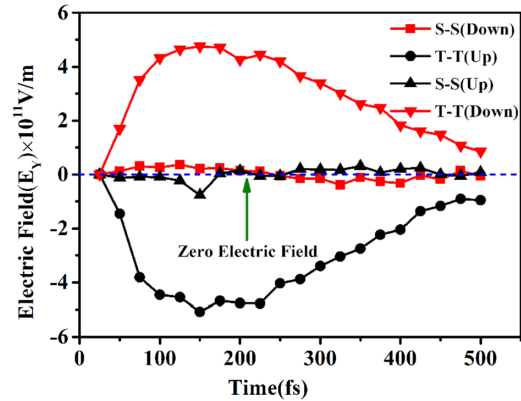

FIG. 3. The average electric field in the up region and the down region for both configurations. In the T–T configuration, the average electric field for the up region is in the negative y direction. In contrast, it is in the positive y direction for the down region. The zero-field line indicates the zero electric field line; for the S–S configuration, the electric field is close to the zero-field line in both regions, resulting in no focusing effect. The average electric field is shown for both plates, and the transient nature of the electric field is reflected here.

accumulated at the vicinity of the plates; after some time; there is a downfall of the electric field, and it eventually reaches nearly zero-field strength. The reduction of electric field is due to the lack of hot electrons in that region as the driving force (laser pulse) vanishes after the pulse duration is reached. As can be observed from the simulation, the proton beam passes across these parallel plate regions in a time range of 100–500 fs, which indicates that the beam meets the strongest electric field (the maximum electric field is observed in a time range between 150 and 250 fs) and gets collimated by it. The observed resultant electric field due to all the available electrons are demonstrated by the simulation is the positive Y direction for the lower Al plate and a negative Y direction for the upper Al plate. There could be some electric field in other direction too; this is the resultant electric field in the two regions due to all hot plasma electrons from Al plates. For the S–S configuration, the obtained electric field is almost close to zero-field line; therefore, the proton beam is unaffected and travels with its inherent divergence. However, in the case of T–T configuration, a very strong net electric field produced from two Al plates makes the proton beam more collimated.

Here, an intense electric field is created by the hot electron plasma of the Al plates. The strength of this electric field E_y is determined by the number of hot electrons that are expelled out of the Al target, which, in turn, depends on how well the laser is absorbed by the target. By tailoring the laser absorption to the target, one can change the number of hot electrons pushed outward from the rear side of the targets (here Al plates). The laser gets absorbed at the critical density surface, and at plasma electron density $n_e = n_c$, the laser delivers most of the energy, resulting in the enormous number of hot electrons accelerated due to the laser energy absorption. Considering the laser propagating in the Y direction with the vibration of the electric field in the X direction, the laser light can be represented in Eq. (1), where w is the

$$\vec{E} = \hat{x} E_0 e^{i\frac{wy}{c}\sqrt{\left(1 - \frac{x^2}{z_r^2}\right)}} e^{-iwt} \tag{1}$$
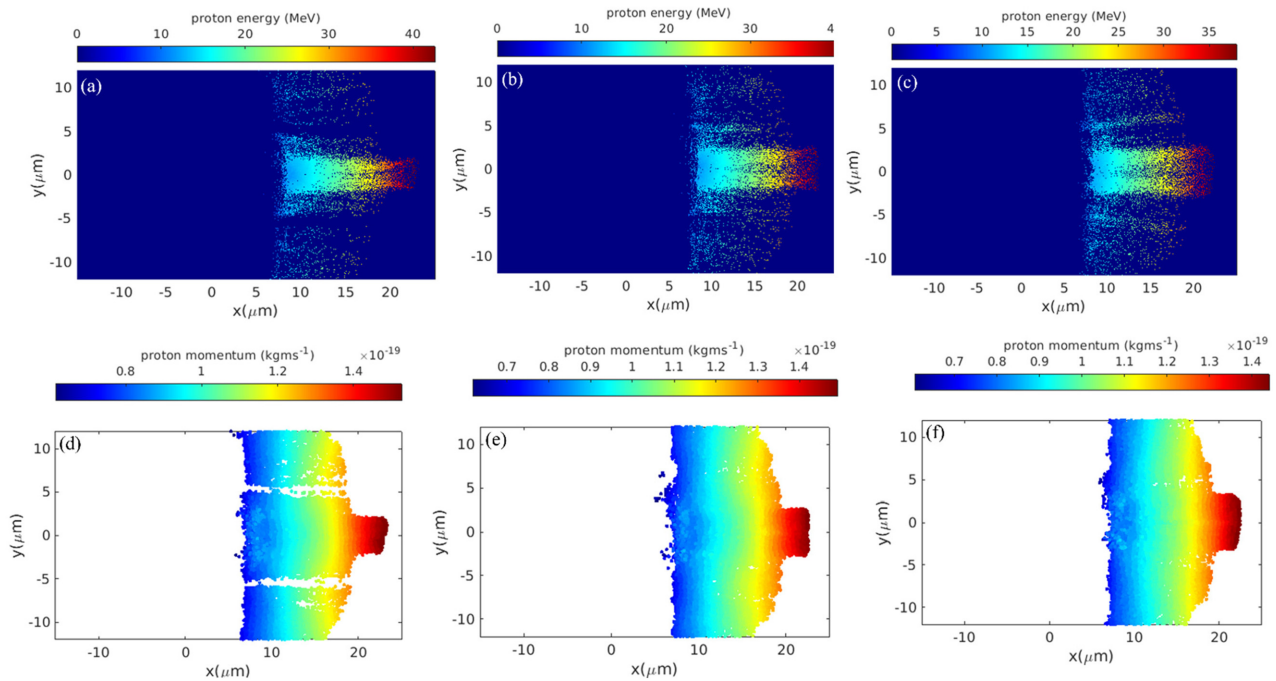
FIG. 4. Energy and momentum distribution shown for the T–T configuration for different densities. The proton energy distribution for the Al target plasma electron density of 10, 20, and 52n_c is shown in (a), (b), and (c), respectively. (d), (e), and (f) The momentum (P_x) distribution for the plasma electron density of 10, 20, and 52n_c, respectively. All the snapshots are taken at 500 fs.

angular frequency for the wavelength of light. We can see from the aforementioned equation, it is the refractive index, $n = \sqrt{1 - \frac{n_e^2}{n_c^2}}$, which plays an important role in the absorption of the laser light into the plasma. This section is concentrated on the impact of plasma electron density of Al plates on proton beam collimation. The plasma electron density for the Au target is also taken to be the same as before. Keeping the laser parameters and the Au target parameters the same, here, we have changed the plasma electron density for Al plates from 10 to 20n_c and 52n_c. Figures 4(a)–4(c) show the proton energy distribution for the Al target plasma electron density of 10, 20, and 52n_c, respectively, for the T–T configuration. The focusing effect is observed to vary with respect to change in Al plasma electron densities. Figures 4(d)–4(f) show the momentum distribution for these three densities for the T–T configuration. The proton beam is found to be more focused for plasma electron densities of 10n_c compared to 52n_c, and for the plasma electron density of 20n_c, the focusing effect is prominent between the densities of 10 and 52n_c. With an increase in plasma electron density, the focusing effect is seen to diminish. Figures 4(d)–4(f) clearly demonstrate that the white gap in the momentum space is significantly more pronounced for the density of 10n_c compared to the densities of 20 and 52n_c. This observation can be attributed to the higher focusing electric field present in the 10n_c density case, which results in an increased push of the proton beam toward the center as compared to the other densities. In Fig. 5, the angular distribution of protons is compared for the S–S and T–T configurations as well as for the various plasma electron densities of Al plates in T–T configuration. When comparing the angular spread of the proton

beam in the two scenarios, the T–T configuration exhibits less spreading than the S–S scenarios. In the T–T case, the beam spreading is lowest for Al plasmas electron density of 10n_c in a comparison to the 20 and 52n_c. Proton angular spread is found to increase with increasing densities of electrons of Al plate produced plasmas, which is already reflected in the proton energy and momentum distribution shown in Fig. 4. The E_y of the hot electrons from the Al plates is responsible for the proton focus. This is confirmed by computing the E_y field for various plasma electron densities.
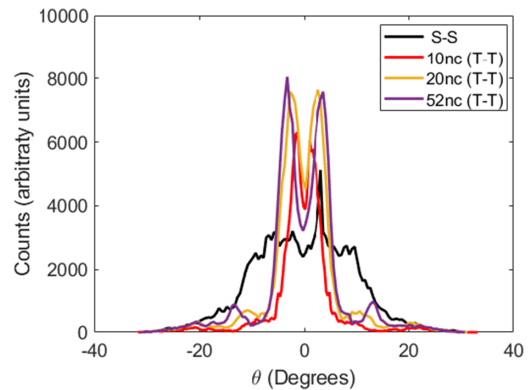

FIG. 5. The proton angular distribution is shown for S–S and T–T configurations. The focusing effect for different Al plasma electron densities is studied for the T–T configuration. This angular distribution is calculated at 500 fs.

Figure 6 illustrates the simulation-derived electric field E_y in the up and down regions for various plasma electron densities. The electric field is higher for plasmas with electron densities of $10n_c$ compared to the electric fields obtained for electron densities of 20 and $52n_c$. The focusing effect follows the same trend since the electric field changes with density. This higher electric field for the plasma electron density of $10n_c$ makes the proton beam more collimated compared to the collimation for other densities considered here. This density dependency of the focusing can be well understood from the absorption mechanism referring to Eq. (1). For $n_e < n_c$, the laser becomes transparent to the target, but for the $n_e > n_c$, the laser becomes opaque to the target. In our work, over dense plasma is considered, where the electron density is a crucial factor in the laser absorption. From Eq. (1), it is obvious that when the value of n_e/n_c is greater than the laser, the penetration depth inside the target is lower, which leads to less absorption of light resulting in lower number of hot electrons available for producing the electric field for collimation. The lower value of n_e/n_c for $n_e = 10n_c$ allows the laser light to be more absorbed in the Al target, leading to the generation of more electrons for producing the electric field for collimation. The evolution of the angular distribution of the proton with respect to time is also studied here for Al plasma electron density of $10n_c$. The corresponding results are shown in Fig. 7. Since the protons accelerated from the gold target enter the external parallel plate regions at about 100 fs, the evolution of angular distribution is considered from 100 fs. From the aforementioned results, it is clear that the angular spread was initially very large. However, as soon as the electric field is established following the interaction of two additional lasers with Al plates, the protons focus owing to the electric field created by the hot plasma electrons. At the start, the number of electrons involved in the generation of electric field is low, with the increase in the interaction time, the number of electrons becomes larger, and the transient nature of the electric field is reflected in the time evolution of the angular distribution of the proton.

The aforementioned results suggest that a strong electric field of the order of 10^{11} V/m is observed to collimate the MeV range proton beam. The focusing effect can be tuned by tuning the electric field. So far, we have witnessed changing the electric field by varying the laser absorption, and it has been demonstrated that the proton beam is more focused for lower plasma electron densities. For all of our
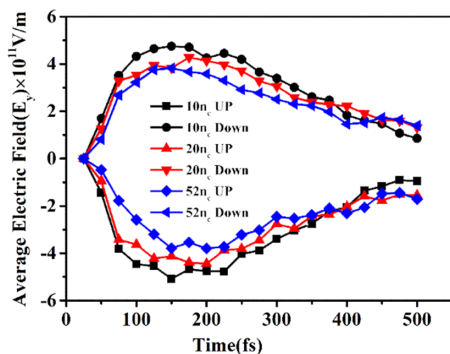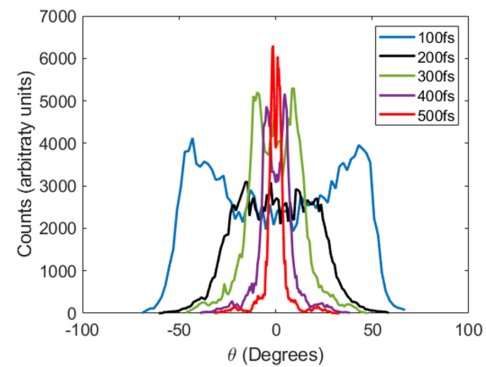

FIG. 7. Time evolution of angular distribution of the proton beam with time is shown here. The density of the Al plasma electron density is considered here to be $10n_c$.

previous results, the separation between the two Al plates was 10 μm, and the separation between two plates is now altered to 16 and 20 μm while leaving all other laser and target parameters unchanged. The plasma electron densities for Al plates are kept at $10n_c$. Figures 8(a)–8(c) depict the energy distribution of the proton beam for the plate separation of 10, 16, and 20 μm, respectively. When comparing plate separations of 10, 16, and 20 μm, it is shown that the proton beam is more tightly focused for the 10 μm plate separation. Figures 8(d)–8(f) show the momentum distribution (P_x) of the proton beam, which reflects the same result. The electric field for different plate separations is obtained for two different regions of interest, the up region and the down region, which is shown in Fig. 9. It is noted that the obtained electric field, which is necessary for beam focusing, is in the negative y direction for the upper Al plate and the positive y direction for the lower plate. In comparison to the 16 and 20 μm separations, a stronger electric field is seen with a 10 μm separation. While the electric field for a plate separation of 16 μm is in the median of values for 10 and 20 μm, it is substantially smaller for a plate separation of 20 μm. This trend of the electric field is also replicated in the focusing effect; due to the higher electric field for 10 μm plate separation, the protons are getting more focused, whereas the focusing effect started decreasing with the increasing plate separations. We can see that for the plate separation of 20 μm, the electric field is almost close to the electric field obtained for the single laser-single target (SS) configuration. The proton beam profile for this configuration is nearly identical to the S–S case [Fig. 2(a)]. Since all the laser and target parameters are same, it is expected to have the same absorption of laser and the same number of electron productions as before. These electrons are the responsible for the supplying of the vertical component of the electric field for the focusing of the proton beam. The magnitude of the electric field varies as inversely square of the distances; as we move away the plates from each other, even though the number of electrons are same, the field decreases due to an increase in the plates separation.

The Al plates length is increased from 10 to 15 and 20 μm while maintaining the initial position same as before. All the laser and target parameters are kept same as before. The proton energy distribution for lengths of 10, 15, and 20 μm is shown in Figs. 10(a)–10(c), respectively. Figures 10(d)–10(f) show the momentum distribution for all three different lengths of Al plates. The results highlight the different
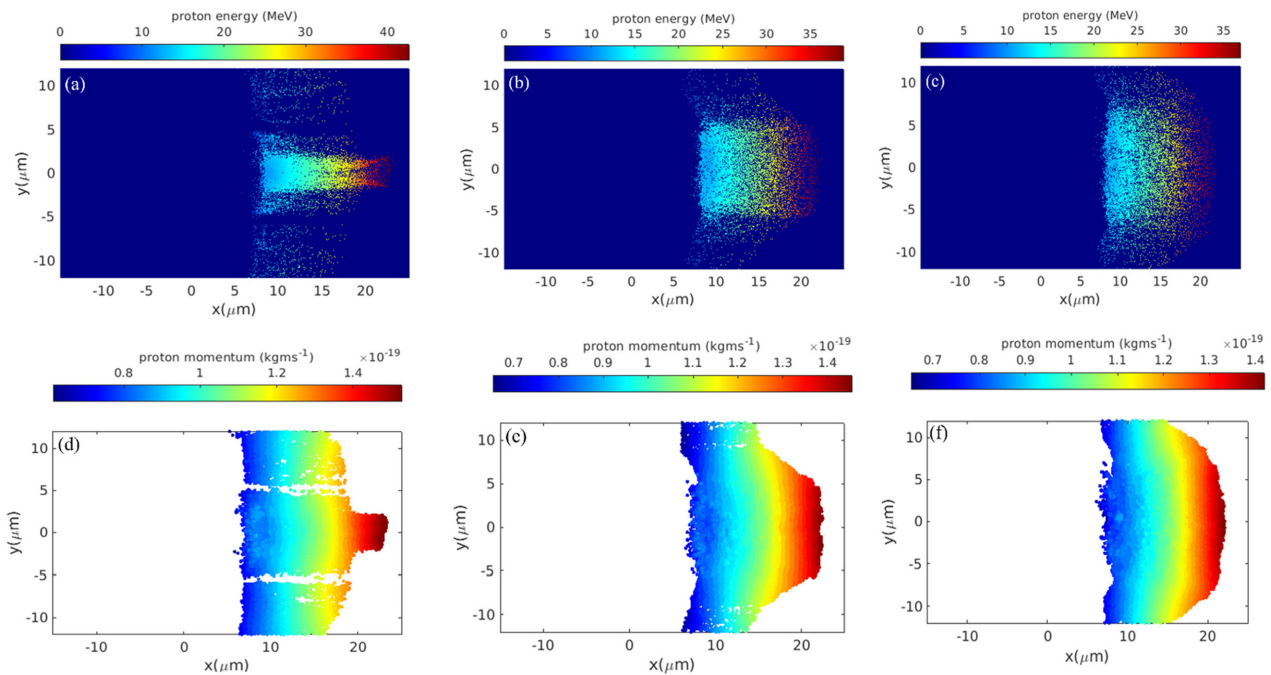

FIG. 6. The density dependency on the focusing effect is presented here, and the electric field (E_y) is shown for both the up region and down region for three different Al plasma electron densities.

FIG. 8. Energy and momentum distribution shown for the T–T configuration for different separation between Al plates of plasma electron density of $10n_c$. (a)–(c) The proton energy distribution for the plates with a separation of 10, 16, and 20 μm, respectively. (d), (e), and (f) The momentum (P_x) distribution for the plates with a separation of 10, 16, and 20, respectively.

focusing effects for the different lengths. It is observed that the 20 μm Al plates have highest degree of proton beam collimation, and the 15 μm Al plates have a relatively higher degree of focusing when compared to the 10 μm plates. Another interesting result, which is depicted here, is that for the length of 10 μm, two proton peaks are seen. These focusing peaks are caused by two different strong electric fields from the two Al plates; however, for the lengths of 15 and 20 μm, the two peaks converge to form a single peak. The angular distribution of the proton for three different lengths is shown in Fig. 11. For the plate length of 20 μm, a single prominent peak is observed compared to

FIG. 9. The simulation obtained electric field (E_y) in the up region and down region is shown for various plate separations (10, 16, and 20 μm).

other lengths. The reason behind this collimation is that the higher plates length enables the proton beam to remain in the plate region for a longer period of time; the longer the plate, the longer the region of electric field; because of the longer traversing region, the protons get pushed into the smaller region toward the center; therefore, the protons appear to have a single peak.

Energy enhancement of the proton beam has also been observed in T–T configuration in comparison to the S–S configuration. The obtained maximum proton energy for the S–S configuration is 30 MeV, and for the T–T configuration, it is 42.5, 40.6, and 37.9 MeV for the Al plasma electron density of 10, 20, and $52n_c$, respectively. Figure 12 depicts the proton energy spectrum for both configurations. It also depicts the spectrum for the T–T arrangement for various Al plasma electron densities. The energy enhancement is observed for all the plasma electron densities for the T–T configuration compared to the S–S configuration. The reason for the energy enhancement is the x component of the electric field (E_x) produced by the electrons coming out from the Al plates. The TNSA field, which results from the charge separation between the heavy ions and electrons at the target's rear side, accelerates protons away from the gold target, and this TNSA field is the target and laser dependent. Since we employed the same target (Au) and laser parameters in all of our configurations, the TNSA field for proton acceleration at the Au target surface will be the same for all the configurations. In the S–S configuration, the 30 MeV energy proton is generated from the TNSA field produced at the rear side of the gold target. The proton energy is observed to be higher in the T–T configuration. In this arrangement, accelerated protons from the gold target enter the zone between two parallel plates of aluminum,
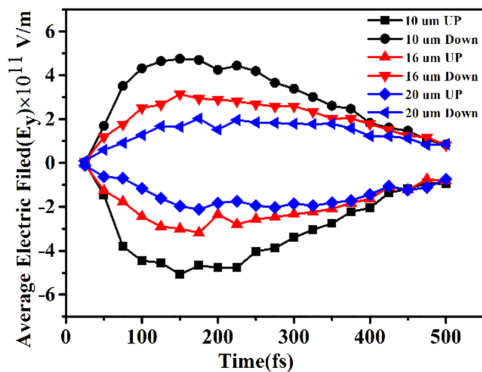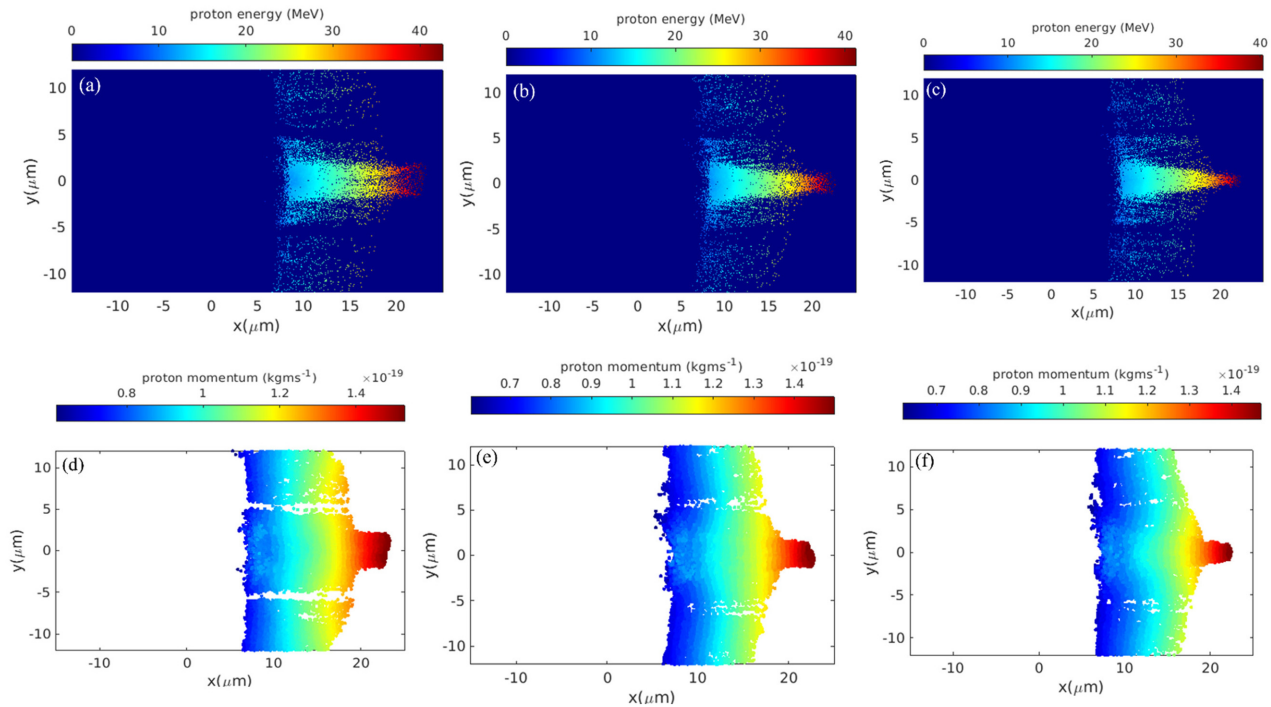
FIG. 10. Energy and momentum distribution shown for the T–T configuration for Al plates of different lengths for plasma electron density of 10n$_c$. (a)–(c) The proton energy distribution for the plates with lengths of 10, 15, and 20 μm, respectively. (d)–(f) The momentum (P$_x$) distribution for the Al plates of different lengths of 10, 16, and 20 μm, respectively.

and the energy is boosted by the additional E$_x$ field created around the aluminum plates. To check whether the energy enhancement is happening inside the parallel plate region or not, we have obtained the maximum proton energy at different time steps for both configurations as shown in Fig. 13(a).

Prior to the beam traversing the parallel plate regions, we can observe that the maximum proton energy is nearly same for both arrangements; however, once the proton beam approaches the region of two parallel plates, the energy enhancement begins in a linear pattern. This infers that the energy enhancement is only due to the parallel plates. From Fig. 13(a), it is clear that in the case of S–S configuration, the maximum proton energy becomes nearly constant after 200 fs, implying that the beams already have gained energy from the TNSA field produced at the rear side of the Au target. However, there is a tendency for energy to increase over time in the scenario of T–T configuration, leading to the conclusion that this energy augmentation is caused by an electric field other than the TNSA field. We calculated the resultant x component of the electric field (E$_x$) in the region extending from the start of the Al plates to the end of the simulation box for both of our configurations to validate that the energy
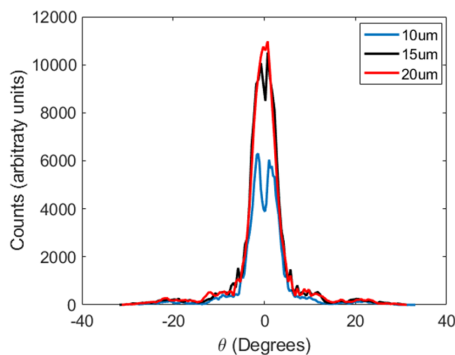

FIG. 11. The proton angular distribution is shown for different Al plate lengths for the T–T configurations. This angular distribution is calculated at 500 fs.
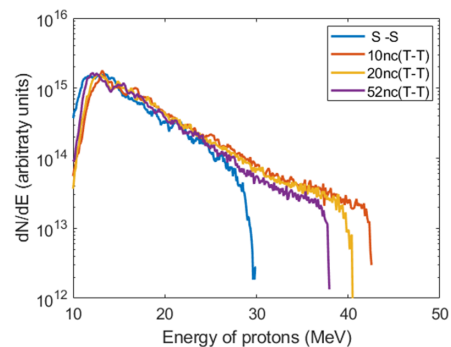

FIG. 12. Proton energy spectrum for S–S and T–T configurations. For the T–T configuration, the energy spectrum is shown for the different plasma electron densities.
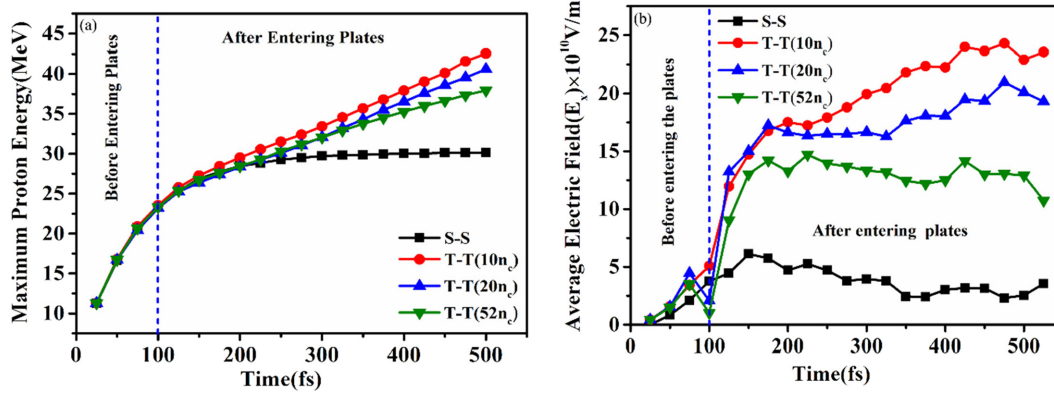
FIG. 13. (a) Maximum proton energies are shown for different timescales for two different scenarios (S–S and T–T). (b) The average horizontal electric field at different time-scales is also studied for these two configurations.

augmentation only begins at the region of the parallel plates. The reason for calculating the electric field till the end of the simulation box is that the E_x exists till the end of the simulation box to accelerate the proton. Figure 13(b) highlights the average horizontal component of the electric field (E_x) for the S–S and T–T configurations. For the T–T configuration, the electric field (E_x) is also calculated for different plasma electron densities of Al plates. The calculated electric field is found to be almost constant for the S–S configuration. When compared to the electric field obtained for the S–S configuration, a larger horizontal electric field is seen in the T–T configuration. This additional electric field is the main factor contributing to the increased proton energy in the T–T configuration. The proton originates from the identical Au target in both scenarios, and the TNSA field created by the gold plasma is the same in both the configurations. In Fig. 13(b), the electric field is calculated in the region starting from the parallel plates to the end of the simulation box, which is the 8-μm distance from the Au target. Even though the TNSA field is created at the gold target's backside, it will still contain some components in this region of interest, which reflects the flat like electric field obtained for the S–S configuration. However, the electric field for the T–T configuration is increasing with the time as can be seen in Fig. 13(b), which combines the TNSA field component, and the electric field generated by the electrons from the aluminum plates. The used electric field for the proton energy enhancement can be calculated by subtraction of the electric field for the S–S configuration from the obtained electric field for the T–T configuration.

The positive electric field (E_x) observed in this study is attributed to plasma electrons generated from the Al plates. In our 2D simulations, we focused on analyzing the E_x and E_y components of the electric field, which are responsible for the electric fields resulting from plasma expansion when the Al plates interact with secondary lasers. The transverse component (E_y) collimates the proton beam, while the horizontal component (E_x) enhances proton energy. Despite the electrons being mainly expelled in the Y direction, a finite component is observed in the X direction. The magnitude of the average electric field (E_x) resulting from plasma expansion is presented in Fig. 13(b). The horizontal electric field (E_x) distribution, shown in Fig. 14, reveals a positive electric field of approximately 10^{11} V/m at the exit end of the Al plates,

indicating that this additional component originates from the Al plate end and is responsible for proton energy enhancement.

Figure 13 points to another significant observation, which is the effect of Al plasma density on proton energy. The proton energy is 42.5 MeV for an electron density of $10n_c$, whereas it is 40.6 and 37.9 MeV, respectively, for the plasma electron density of 20 and $52n_c$. Equation (1) clearly illustrates how the Al plasma electron density influences the laser absorption in the Al target, which is already discussed previously. For lesser Al plasma electron densities, the absorption becomes higher leading to higher number of electrons available for generating the horizontal component of the electric field for enhancing the energy of the proton beam.

DISCUSSION

What has been discussed thus far is that the plasma density plays an important role in controlling the divergence and energy of the proton beam as inferred from Figs. 5 and 12. The electron density was varied from lower to higher density ($10–52n_c$) to observe the impact on the laser absorption at different electron densities. It is observed that for lower density plasma (10 and $20n_c$), more laser absorption
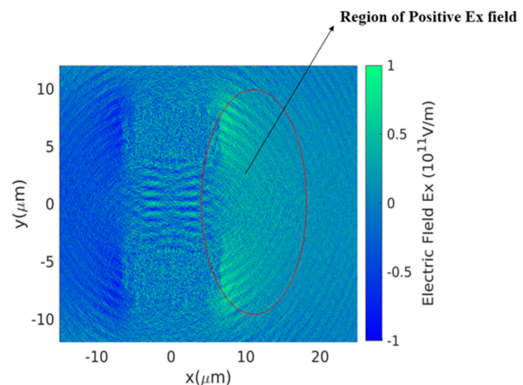

FIG. 14. This illustrates the distribution of the longitudinal electric field, with a specific region of positive electric field highlighted. This positive electric field is responsible for enhancing the energy of the proton beam.

results in the production of more electrons for the formation of the electric field, which further enhances the beam quality in terms of energy and collimation. Though the electron density $52n_c$ corresponds to the actual solid density for Al target, lower density Al plasma (10 and $20n_c$) could be achieved by introducing a pre-plasma before the cold Al target. Before the main pulse, it is the pre-pulse that interacts with the target first and create an exponential density gradient. The main pulse then interacts with the preformed pre-plasma by the pre-pulse. To date, the thickness of the Al is kept 2 μm with uniform densities 52, 20, and $10n_c$. Keeping the whole target thickness the same (2 μm), a combination of pre-plasma (thickness of 1 μm) at the front attached with a solid density target of $52n_c$ (thickness of 1 μm) at the rear side is considered. In one case, a pre-plasma of scale length 1 μm with an exponential density profile varying from 10 to $52n_c$ is attached along with an Al plasma layer of thickness 1 μm with uniform density $52n_c$. In another case, we have considered the same configuration with density varying from 20 to $52n_c$ for 1 μm pre-plasma. Figures 15(a) and 15(b) show the plasma density profile for Al plates, respectively, for 10 and $20n_c$ after introducing the pre-plasma in both the cases.

Figures 16(a) and 16(b) show the proton energy beam profile for the pre-plasma density starting from the 10 and $20n_c$, respectively. It is observed that, the proton energy collimation is almost same as compared to the corresponding uniform low plasma densities of 10 and $20n_c$ [Figs. 4(a) and 4(b)]. Figure 16(c) shows the proton energy spectrum for the two cases—a uniform low-density Al plasma ($10n_c$) and a pre-plasma density profile with density variation from 10 to $52n_c$ attached with a solid density plasma of $52n_c$.

The cutoff energy for the proton beam at 550 fs is 43.08 and 42.52 MeV, respectively, for the case with pre-plasma and without pre-plasma. Figure 16(d) shows the proton energy spectrum for the low-density uniform plasma of $20n_c$ and a pre-plasma density profile with density variation from 20 to $52n_c$ attached with a solid density plasma of $52n_c$. The proton cutoff energies are 40.70 and 40.58 MeV, respectively, for the case with pre-plasma and without pre-plasma. The collimation and the proton energies are same for the pre-plasma cases in comparison to the low-density uniform plasma cases. These results suggest that even after introducing a low-density pre-plasma in front

of high-density plasma ($52n_c$), we can achieve the same energy as in the case of low-density uniform plasma. With experimental point of view, though these low-density plasmas may not be directly producible for Al, a suitable pre-pulse could be used to introduce a pre-plasma gradient at the front side enabling similar control over the collimation and energy of the proton beam.

Due to limitations in computational resources, our manuscript only presents results from a 2D simulation. However, our proposed approach can be extended to a more realistic 3D scheme, where a hollow cylindrical target could be used instead of two parallel plates. To achieve proper collimation and beam shape, it is essential to maintain a symmetric electric field. In the 3D scheme, this can be accomplished by using multiple laser beams positioned opposite to each other around the circumference of the cylinder. Tuning of energy and collimation could be achieved by adjusting the intensity of the secondary lasers. Current laser facilities have the capability to provide multiple laser beams of suitable intensities, and also beam splitting optics could be used to derive the secondary laser pulses from the main laser pulse. The energy of the secondary pulses could be one or two orders of magnitude lesser compared to the main pulse energy. Previous work by Murakami et al.[48] has reported the production of an axial sheath field using multiple laser beams. In their simulations, a microtube with a cylindrical shape was used to interact with the laser pulses, which produced a sheath field in the vacuum space within the cylinder. Although the objective of their work was different, the sheath field pointing toward the axis of the cylinder was observed, which is similar to what is expected from a 3D configuration of our proposed scheme.

In the simulations, the Au target is positioned at the boundary of the simulation box. However, since the laser also begins at the boundary, it covers two cells to initiate the laser propagation. This could lead to variations in the corresponding results. To maintain the correctness of our approach, the proton energy has been compared for two cases: one where the target was kept at the simulation box boundary and another where the target is shifted from the boundary by 50 nm. In the first case, the maximum proton energy was 30.1 MeV, and in the
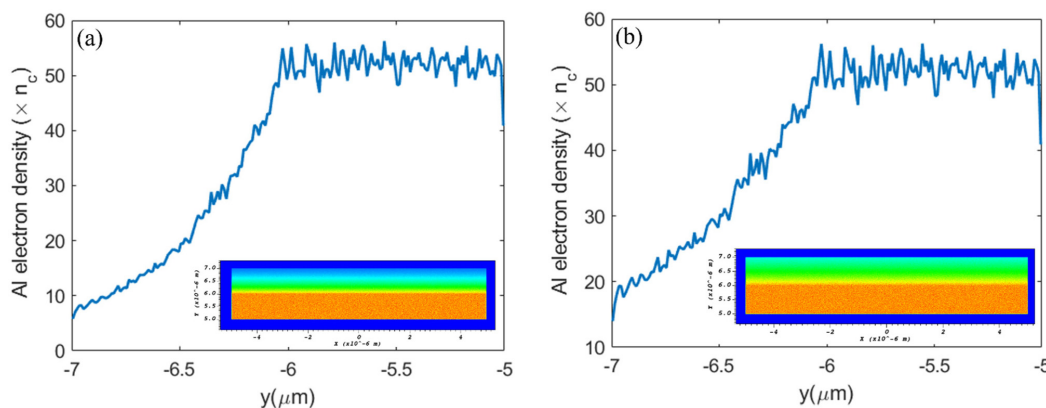

FIG. 15. (a) The Al plasma density profile after introducing a pre-plasma of 1 μm length having density ranging from 10 to $52n_c$, with solid density target ($52n_c$) at backside. (b) The Al plasma density profile after introducing a pre-plasma of 1 μm length having density ranging from 20 to $52n_c$, with solid density target ($52n_c$) at backside. The corresponding two-dimensional Al plasma is shown in the inset of both the figures.
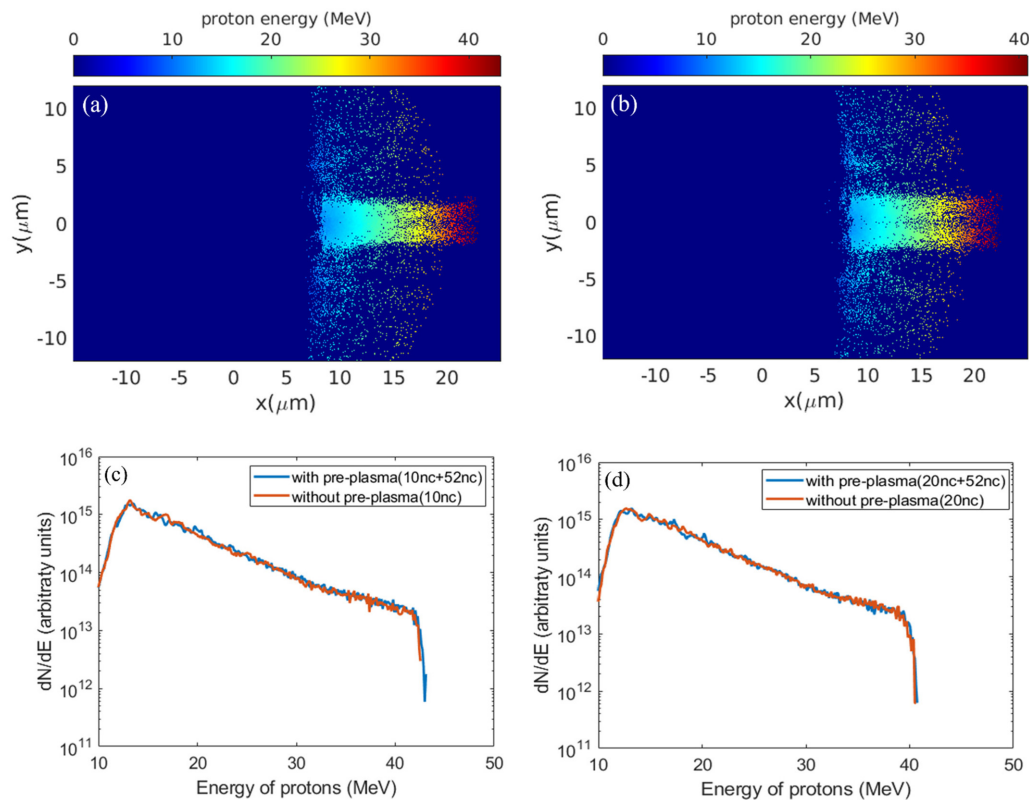
FIG. 16. (a) Energy distribution of the proton beam for the pre-plasma condition ranging from 10 to $52n_c$. (b) Energy distribution of the proton beam for the pre-plasma condition ranging from 20 to $52n_c$. (c) Energy spectrum compared between a uniform electron density of $10n_c$ and pre-plasma density ranging from 10 to $52n_c$. (d) Energy spectrum compared between a uniform electron density of $20n_c$ and pre-plasma density ranging from 20 to $52n_c$.

second case, it was 29.8 MeV. We observed no significant difference in the proton energy, indicating the correctness of the simulations.

CONCLUSIONS

The proposed three laser configuration enhances the proton focusing as well as the energy. The protons from the gold target are focused due to the vertical electric field, and energy enhancement is due to the horizontal electric field created by the parallel Al plates. These electric fields (E_x and E_y) with magnitude of the order of 10^{11} V/m are generated from the plasma electrons from the Al plates interacting with another two secondary lasers. This model is very flexible in tuning the energy as well as the divergence of the proton beam. The target and laser parameters play an important role in controlling the beam properties. This configuration is useful for the cancer therapy and proton fast ignition in inertial confinement fusion.

AUTHOR DECLARATIONS
Conflict of Interest

The authors have no conflicts to disclose.

Author Contributions

Kousik Makur: Conceptualization (equal); Data curation (equal); Formal analysis (equal); Investigation (equal); Methodology (equal); Writing – original draft (equal); Writing – review & editing (equal). **Santhosh Krishnamurthy:** Conceptualization (equal); Data curation (equal); Formal analysis (equal); Methodology (equal); Writing – original draft (equal); Writing – review & editing (equal). **Bhuvanesh Ramakrishna:** Conceptualization (equal); Methodology (equal); Project administration (equal); Supervision (equal); Writing – original draft (equal); Writing – review & editing (equal).

DATA AVAILABILITY

The data that support the findings of this study are available from the corresponding author upon reasonable request.

REFERENCES

[1]M. Thévenet, A. Leblanc, S. Kahaly, H. Vincenti, A. Vernier, F. Quéré, and J. Faure, "Vacuum laser acceleration of relativistic electrons using plasma mirror injectors," Nat. Phys. **12**(4), 355–360 (2016).

[2]A. Macchi, M. Borghesi, and M. Passoni, "Ion acceleration by superintense laser-plasma interaction," Rev. Mod. Phys. **85**(2), 751–793 (2013).

[3]H. Daido, M. Nishiuchi, and A. S. Pirozhkov, "Review of laser-driven ion sources and their applications," Rep. Prog. Phys. **75**(5), 056401 (2012).

[4]E. L. Clark, K. Krushelnick, J. R. Davies, M. Zepf, M. Tatarakis, F. N. Beg, A. Machacek, P. A. Norreys, M. I. K. Santala, I. Watts, and A. E. Dangor, "Measurements of energetic proton transport through magnetized plasma from intense laser interactions with solids," Phys. Rev. Lett. **84**, 670 (2000).

[5]W. Theobald, K. Akli, R. Clarke, J. A. Delettrez, R. R. Freeman, S. Glenzer, J. Green, G. Gregori, R. Heathcote, N. Izumi, J. A. King, J. A. Koch, J. Kuba, K. Lancaster, A. J. MacKinnon, M. Key, C. Mileham, J. Myatt, D. Neely, P. A. Norreys, H. S. Park, J. Pasley, P. Patel, S. P. Regan, H. Sawada, R. Shepherd, R. Snavely, R. B. Stephens, C. Stoeckl, M. Storm, B. Zhang, and T. C. Sangster, "Hot surface ionic line emission and cold K-inner shell emission from petawatt-laser-irradiated Cu foil targets," Phys. Plasmas **13**(4), 043102 (2006).

[6]F. Girard, "Review of laser produced multi-keV X-ray sources from metallic foils, cylinders with liner, and low density aerogels," Phys. Plasmas **23**(4), 040501 (2016).

[7]Y. J. Gu, M. Jirka, O. Klimo, and S. Weber, "Gamma photons and electron-positron pairs from ultra-intense laser-matter interaction: A comparative study of proposed configurations," Matter Radiat. At. Extremes **4**(6), 064403 (2019).

[8]R. A. Snavely, M. H. Key, S. P. Hatchett, T. E. Cowan, M. Roth, T. W. Phillips, M. A. Stoyer, E. A. Henry, T. C. Sangster, M. S. Singh, S. C. Wilks, A. Mackinnon, A. Offenberger, D. M. Pennington, K. Yasuike, A. B. Langdon, B. F. Lasinski, J. Johnson, M. D. Perry, and E. M. Campbell, "Intense high-energy proton beams from petawatt-laser irradiation of solids," Phys. Rev. Lett. **85**, 2945 (2000).

[9]A. Higginson, R. J. Gray, M. King, R. J. Dance, S. D. R. Williamson, N. M. H. Butler, R. Wilson, R. Capdessus, C. Armstrong, J. S. Green, S. J. Hawkes, P. Martin, W. Q. Wei, S. R. Mirfayzi, X. H. Yuan, S. Kar, M. Borghesi, R. J. Clarke, D. Neely, and P. McKenna, "Near-100 MeV protons via a laser-driven transparency-enhanced hybrid acceleration scheme," Nat. Commun. **9**(1), 724 (2018).

[10]L. Lecherbourg, I. Lantuéjoul, B. Vauzour, P. E. Masson-Laborde, X. Davoine, N. Blanchot, J. L. Dubois, X. Vaisseau, E. d'Humières, L. Gremillet, A. Duval, Ch. Reverdin, B. Rosse, G. Boutoux, J. E. Ducret, Ch. Rousseaux, V. Tikhonchuk, and D. Batani, Matter Radiat. Extremes **6**, 056901 (2021).

[11]V. Malka, S. Fritzler, E. Lefebvre, E. D'Humières, R. Ferrand, G. Grillon, C. Albaret, S. Meyroneinc, J. P. Chambaret, A. Antonetti, and D. Hulin, "Practicability of protontherapy using compact laser systems," Med. Phys. **31**(6), 1587–1592 (2004).

[12]S. Bulanov, T. Esirkepov, V. Khoroshkov, A. Kuznetsov, and F. Pegoraro, "Oncological hadrontherapy with laser ion accelerators," Phys. Lett. A **299**, 240–247 (2002).

[13]E. Fourkal, B. Shahine, M. Ding, J. S. Li, T. Tajima, and C. M. Ma, "Particle in cell simulation of laser-accelerated proton beams for radiation therapy," Med. Phys. **29**(12), 2788–2798 (2002).

[14]M. Borghesi, D. H. Campbell, A. Schiavi, M. G. Haines, O. Willi, A. J. MacKinnon, P. Patel, L. A. Gizzi, M. Galimberti, R. J. Clarke, F. Pegoraro, H. Ruhl, and S. Bulanov, Phys. Plasmas **9**, 2214–2220 (2002).

[15]G. Liao, Y. Li, B. Zhu, Y. Li, F. Li, M. Li, X. Wang, Z. Zhang, S. He, W. Wang, F. Lu, F. Zhang, L. Yang, K. Zhou, N. Xie, W. Hong, Y. Gu, Z. Zhao, B. Zhang, and J. Zhang, "Proton radiography of magnetic fields generated with an open-ended coil driven by high power laser pulses," Matter Radiat. At. Extremes **1**(4), 187–191 (2016).

[16]K. F. F. Law, M. Bailly-Grandvaux, A. Morace, S. Sakata, K. Matsuo, S. Kojima, S. Lee, X. Vaisseau, Y. Arikawa, A. Yogo, K. Kondo, Z. Zhang, C. Bellei, J. J. Santos, S. Fujioka, and H. Azechi, "Direct measurement of kilo-tesla level magnetic field generated with laser-driven capacitor-coil target by proton deflectometry," Appl. Phys. Lett. **108**(9), 091104 (2016).

[17]M. Tabak, J. Hammer, M. E. Glinsky, W. L. Kruer, S. C. Wilks, J. Woodworth, E. M. Campbell, M. D. Perry, and R. J. Mason, "Ignition and high gain with ultrapowerful lasers," Phys. Plasmas **1**(5), 1626–1634 (1994).

[18]P. Mora, "Plasma expansion into a vacuum," Phys. Rev. Lett. **90**(18), 185002 (2003).

[19]S. C. Wilks, A. B. Langdon, T. E. Cowan, M. Roth, M. Singh, S. Hatchett, M. H. Key, D. Pennington, A. MacKinnon, and R. A. Snavely, "Energetic proton generation in ultra-intense laser-solid interactions," Phys. Plasmas **8**(2), 542–549 (2001).

[20]L. A. Gizzi, D. Giove, C. Altana, F. Brandi, P. Cirrone, G. Cristoforetti, A. Fazzi, P. Ferrara, L. Fulgentini, P. Koester, L. Labate, G. Lanzalone, P. Londrillo, D. Mascali, A. Muoio, D. Palla, F. Schillaci, S. Sinigardi, S. Tudisco, and G. Turchetti, "A new line for laser-driven light ions acceleration and related TNSA studies," Appl. Sci. (Switzerland) **7**(10), 984 (2017).

[21]K. Zeil, J. Metzkes, T. Kluge, M. Bussmann, T. E. Cowan, S. D. Kraft, R. Sauerbrey, and U. Schramm, "Direct observation of prompt pre-thermal laser ion sheath acceleration," Nat. Commun. **3**, 874 (2012).

[22]M. Allen, P. K. Patel, A. Mackinnon, D. Price, S. Wilks, and E. Morse, "Direct experimental evidence of back-surface ion acceleration from laser-irradiated gold foils," Phys. Rev. Lett. **93**(26 I), 265004 (2004).

[23]S. J. Gitomer, R. D. Jones, F. Begay, A. W. Ehler, J. F. Kephart, and R. Kristal, "Fast ions and hot electrons in the laser–plasma interaction," Phys. Fluids **29**(8), 2679 (1986).

[24]L. Romagnani, J. Fuchs, M. Borghesi, P. Antici, P. Audebert, F. Ceccherini, T. Cowan, T. Grismayer, S. Kar, A. MacChi, P. Mora, G. Pretzler, A. Schiavi, T. Toncian, and O. Willi, "Dynamics of electric fields driving the laser acceleration of multi-MeV protons," Phys. Rev. Lett. **95**(19), 195001 (2005).

[25]H. Alfvén, Phys. Rev. **55**, 425 (1939).

[26]Y. Sentoku, K. Mima, S. I. Kojima, and H. Ruhl, "Magnetic instability by the relativistic laser pulses in overdense plasmas," Phys. Plasmas **7**(2), 689–695 (2000).

[27]I. Y. Dodin and N. J. Fisch, "Correction to the Alfvén-Lawson criterion for relativistic electron beams," Phys. Plasmas **13**, 103104 (2006).

[28]A. R. Bell and R. J. Kingham, "Resistive collimation of electron beams in laser-produced plasmas," Phys. Rev. Lett. **91**(3), 035003 (2003).

[29]M. S. Wei, F. N. Beg, E. L. Clark, A. E. Dangor, R. G. Evans, A. Gopal, K. W. D. Ledingham, P. McKenna, P. A. Norreys, M. Tatarakis, M. Zepf, and K. Krushelnick, "Observations of the filamentation of high-intensity laser-produced electron beams," Phys. Rev. E **70**, 056412 (2004).

[30]J. Fuchs, T. E. Cowan, P. Audebert, H. Ruhl, L. Gremillet, A. Kemp, M. Allen, A. Blazevic, J. C. Gauthier, M. Geissel, M. Hegelich, S. Karsch, P. Parks, M. Roth, Y. Sentoku, R. Stephens, and E. M. Campbell, "Spatial uniformity of laser-accelerated ultrahigh-current mev electron propagation in metals and insulators," Phys. Rev. Lett. **91**(25), 255002 (2003).

[31]M. Roth, T. E. Cowan, M. H. Key, S. P. Hatchett, C. Brown, W. Fountain, J. Johnson, D. M. Pennington, R. A. Snavely, S. C. Wilks, K. Yasuike, H. Ruhl, F. Pegoraro, S. V. Bulanov, E. M. Campbell, M. D. Perry, and H. Powell, "Fast ignition by intense laser-accelerated proton beams," Phys. Rev. Lett. **86**(3), 436–439 (2001).

[32]B. Ramakrishna, M. Tayyab, S. Bagchi, T. Mandal, A. Upadhyay, S. M. Weng, M. Murakami, T. E. Cowan, J. A. Chakera, P. A. Naik, and P. D. Gupta, "Filamentation control and collimation of laser accelerated MeV protons," Plasma Phys. Control Fusion **57**(12), 125013 (2015).

[33]L. A. Gizzi, S. Betti, E. Förster, D. Giulietti, S. Höfer, P. Köster, L. Labate, R. Lötzsch, A. P. L. Robinson, and I. Uschmann, "Role of resistivity gradient in laser-driven ion acceleration," Phys. Rev. Spec. Top. - Accel. Beams **14**(1), 011301 (2011).

[34]S. Krishnamurthy, K. Makur, and B. Ramakrishna, "Observation of resistive Weibel instability in intense laser plasma," Laser Part. Beams **38**(2), 152–158 (2020).

[35]R. Sonobe, S. Kawata, S. Miyazaki, M. Nakamura, and T. Kikuchi, "Suppression of transverse proton beam divergence by controlled electron cloud in laser-plasma interactions," Phys. Plasmas **12**(7), 073104 (2005).

[36]T. P. Yu, Y. Y. Ma, M. Chen, F. Q. Shao, M. Y. Yu, Y. Q. Gu, and Y. Yin, "Quasimonoenergetic proton beam from ultraintense-laser irradiation of a target with holed backside," Phys. Plasmas **16**(3), 033112 (2009).

[37]Z. Gong, S. S. Bulanov, T. Toncian, and A. V. Arefiev, "Energy-chirp compensation of laser-driven ion beams enabled by structured targets," Phys. Rev. Res. **4**, L042031 (2018).

[38]T. Okada, A. A. Andreev, Y. Mikado, and K. Okubo, "Energetic proton acceleration and bunch generation by ultraintense laser pulses on the surface of thin plasma targets," Phys. Rev. E **74**(2), 026401 (2006).

[39]S. Kar, K. Markey, M. Borghesi, D. C. Carroll, P. McKenna, D. Neely, M. N. Quinn, and M. Zepf, "Ballistic focusing of polyenergetic protons driven by petawatt laser pulses," Phys. Rev. Lett. **106**(22), 225003 (2011).

[40] M. Schollmeier, S. Becker, M. Geißel, K. A. Flippo, A. Blaević, S. A. Gaillard, D. C. Gautier, F. Grüner, K. Harres, M. Kimmel, F. Nürnberg, P. Rambo, U. Schramm, J. Schreiber, J. Schütrumpf, J. Schwarz, N. A. Tahir, B. Atherton, D. Habs, B. M. Hegelich, and M. Roth, "Controlled transport and focusing of laser-accelerated protons with miniature magnetic devices," Phys. Rev. Lett. **101**(5), 055004 (2008).

[41] M. Nishiuchi, I. Daito, M. Ikegami, H. Daido, M. Mori, S. Orimo, K. Ogura, A. Sagisaka, A. Yogo, A. S. Pirozhkov, H. Sugiyama, H. Kiriyama, H. Okada, S. Kanazawa, S. Kondo, T. Shimomura, M. Tanoue, Y. Nakai, H. Sasao, D. Wakai, H. Sakaki, P. Bolton, I. W. Choi, J. H. Sung, J. Lee, Y. Oishi, T. Fujii, K. Nemoto, H. Souda, A. Noda, Y. Iseki, and T. Yoshiyuki, "Focusing and spectral enhancement of a repetition-rated, laser-driven, divergent multi-MeV proton beam using permanent quadrupole magnets," Appl. Phys. Lett. **94**(6), 061107 (2009).

[42] S. Ter-Avetisyan, M. Schnürer, R. Polster, P. V. Nickles, and W. Sandner, "First demonstration of collimation and monochromatisation of a laser accelerated proton burst," Laser Part. Beams **26**(4), 637–642 (2008).

[43] T. Toncian, M. Borghesi, J. Fuchs, E. D'humières, P. Antici, P. Audebert, E. Brambrink, C. A. Cecchetti, A. Pipahl, L. Romagnani, and O. Willi, "Ultrafast laser-driven microlens to focus and energy-select mega-electron volt protons," Science **312**(5772), 410–413 (2006).

[44] O. Willi, T. Toncian, M. Borghesi, J. Fuchs, E. D'humières, P. Antici, P. Audebert, E. Brambrink, C. Cecchetti, A. Pipahl, and L. Romagnani, "Laser triggered micro-lens for focusing and energy selection of MeV protons," Laser Part. Beams **25**, 71–77 (2007).

[45] J. Strehlow, J. Kim, M. Bailly-Grandvaux, S. Bolaños, H. Smith, A. Haid, E. L. Alfonso, C. Aniculaesei, H. Chen, T. Ditmire, M. E. Donovan, S. B. Hansen, B. M. Hegelich, H. S. McLean, H. J. Quevedo, M. M. Spinks, and F. N. Beg, "A laser parameter study on enhancing proton generation from microtube foil targets," Sci. Rep. **12**(1), 10827 (2022).

[46] L. A. Gizzi, E. Boella, L. Labate, F. Baffigi, P. J. Bilbao, F. Brandi, G. Cristoforetti, A. Fazzi, L. Fulgentini, D. Giove, P. Koester, D. Palla, and P. Tomassini, "Enhanced laser-driven proton acceleration via improved fast electron heating in a controlled pre-plasma," Sci. Rep. **11**(1), 13728 (2021).

[47] T. D. Arber, K. Bennett, C. S. Brady, A. Lawrence-Douglas, M. G. Ramsay, N. J. Sircombe, P. Gillies, R. G. Evans, H. Schmitz, A. R. Bell, and C. P. Ridgers, "Contemporary particle-in-cell approach to laser-plasma modelling," Plasma Phys. Control Fusion **57**(11), 113001 (2015).

[48] M. Murakami, J. J. Honrubia, K. Weichman, A. V. Arefiev, and S. V. Bulanov, "Generation of megatesla magnetic fields by intense-laser-driven microtube implosions," Sci. Rep. **10**(1), 16653 (2020).